ADVANCED MATERIALS

[18] H. Kobayashi, R. Kato, A. Kobayashi, G. Saito, M. Tokumoto, H. Anzai, T. Ishiguro, *Chem. Lett*. **1986**, 93.
[19] The single crystals of the $Bu_4NBr_{0.6}I_{1.4}Cl$ salt, were obtained by addition of IBr to a solution of Bu_4NCl in ethanol at a reagent ratio of 1:0.5. Stoichiometry of the anion has been found by EDX. Based on a Raman study the anion consists of the I_2Br^- (band at 140 cm^{-1}), IBr_2^- (band at 150–176 cm^{-1}), $BrICl^-$ (band at 225 cm^{-1}), and ICl_2^- (band at 250–263 cm^{-1}) trihalide anions.
[20] The X-ray diffraction data from single crystals for both trihalide salts were measured using an Enraf Nonius CAD4 diffractometer with graphite monochromatic Mo Kα radiation (λ = 0.71073 Å) at room temperature. Unit cell parameters of the new α‴- crystal were determined from a least-squares analysis of 25 reflections. The intensities of 8106 non-zero reflections were collected by the ω-scan method up to $2\Theta = 50°$. The index range was $-20 < h < 20$, $-10 < k < 10$, $0 < l < 19$. 6093 independent reflections with $I > 2\sigma(I)$, $R_{int} = 0.011$, were used in the structure analysis. Absorption correction was applied using the DIFABS algorithm. The main room temperature crystal data for the single crystal of **1** are as follows: a = 17.116(2), b = 8.956(1), c = 16.338(2) Å, α = 88.09(2), β = 84.22(1), ψ = 81.22(2)°, V = 2462.1(5) $Å^3$, space group $P\bar{1}$, Z = 3, M = 1024.89, d_{calc} = 2.074 g/cm^3, μ = 36.5 cm^{-1}, $F(000)$ = 1507.2. The structure was solved by direct methods using AREN programs (V. I. Andrianov, *AREN-88, The System of Programs for Solving and Refinement of Crystal Structures*, Institute of Crystallography AN SSSR, Moscow, **1988**) and refined by the anisotropic least-squares method for non-hydrogen atoms using the SHELXL-97 program (G. M. Sheldrick, *SHELXL-93, Program for the Refinement of Crystal Structures*, Göttingen University, Germany, **1993**). Mixed occupation of $(Br_{1-x}Cl_x)$ with identification of the x parameter was introduced into the terminal positions of the BrICl anions. Hydrogen atoms were located from difference Fourier maps and some of them (from disordered ethylene groups) were geometrically calculated. Only position parameters of the H-atoms were refined. The structure was refined to R = 0.040. Unit cell parameters of the single crystal at 175 K are as follows a = 5.674(2), b = 9.021(2), c = 16.340(2) Å, α = 92.79(2), β = 97.56(2), ψ = 103.41(3)°, V = 803.7(4) $Å^3$, which are characteristic of metallic β″-type structures [3,25,26]. Parameters of a single crystal of **2** at room temperature are as follows: a = 12.348(2), b = 8.865(1), c = 16.317(2) Å, α = 91.41(2), β = 93.66(2), ψ = 113.44(3)°, V = 1635.7(5) $Å^3$, space group $P\bar{1}$, Z = 2. This crystal is isostructural to the well-known α′- type crystals of BEDT-TTF trihalides [7,18,26].
[21] The content of halides in the crystals of both trihalide salts was determined using EDX. The data were collected for a 4000× magnification at an electrical potential of 20 keV. Element compositions of the crystals were found to be $C_{20}H_{16}S_{16}Br_{1.26}I_{1.14}Cl_{0.60}$ and $C_{20}H_{16}S_{16}Br_{1.29}I_{1.09}Cl_{0.62}$ for α‴- and α′-phases, respectively. The experimental error (Δ) of this estimation of the stoichiometry is equal to 0.1.
[22] S. Sugai, G. Saito, *Solid State Commun*. **1986**, *58*, 759
[23] J. R. Ferraro, M. A. Beno, R. J. Thorn, H. H. Wang, K. S. Webb, J. M. Williams, *J. Phys. Chem. Solids* **1986**, *47*, 301.
[24] R. Wojciechowski, J. Ulanski, S. Lefrant, E. Faulques, E. Laukhina, V. Tkacheva, *J. Chem. Phys.* **2000**, *112*, 7634.
[25] a) L. I. Buravov, A. V. Zvarykina, A. A. Ignat'ev, A. I. Kotov, V. N. Laukhin, M. K. Makova, V. A. Merzhanov, L. P. Rozenberg, R. P. Shibaeva, E. B. Yagubskii, *Izv. Akad. Nauk SSSR, Ser. Khim*. **1988**, 2027; L. I. Buravov, A. V. Zvarykina, A. A. Ignat'ev, A. I. Kotov, V. N. Laukhin, M. K. Makova, V. A. Merzhanov, L. P. Rozenberg, R. P. Shibaeva, E. B. Yagubskii, *Bull. Acad. Sci. USSR (Engl.)* **1988**, *1825.*
[26] According to Scheme 1 the β-$(BEDT\text{-}TTF)_2ICl_2$[25] and α-$(BEDT\text{-}TTF)_2IBr_2$ [7] salts correspond to β″- and α′-type phases, respectively.
[27] O. A. D'yachenko, V. V. Gritsenko, G. V. Shilov, E. I. Zhilyaeva, R. N. Lyubovskaya, *Russ. Chem. Bull*. **1995**, *44*, 883.
[28] A. F. Wells, *Structural Inorganic Chemistry*, 5th ed., Clarendon, Oxford **1984**.

Raman Imaging of Single Carbon Nanotubes**

By *Alf Mews,* Felix Koberling, Thomas Basché, Guenther Philipp, Georg S. Duesberg, Siegmar Roth,* and *Marko Burghard*

Carbon nanotubes (CNTs) have been used as versatile building blocks of electrical devices such as field-effect transistors[1,2] or conductivity sensors.[3] In addition, more advanced device configurations like intramolecular junctions[4] or interconnections between different individual nanotubes,[5] have been realized. However, progress towards reproducible devices implementing these remarkable molecular wires is slowed down by the lack of an effective control over tube diameter and helicity, which determine their metallic or semiconducting behavior.[6] The ability to additionally collect spectroscopic data on specific nanotubes under electric study would therefore strongly contribute to an increased understanding of their electrical properties. Raman scattering has proven to be a powerful tool to probe the structure, diameter and electronic properties of CNTs in bulk samples.[7–9] On the other hand, single-molecule fluorescence spectroscopy has revealed that ensemble measurements show only the average properties of molecules[10,11] or nanoparticles[12] due to various sources of sample inhomogeneities such as structural disorder or size distribution. The possibility of acquiring Raman spectra from individual CNTs has been demonstrated for tubes deposited on metal substrates suitable for surface enhanced Raman scattering (SERS),[13] and even without surface enhancement techniques on glass substrates.[14] On this basis, we report for the first time the imaging of tubes by use of scanning confocal Raman microscopy as an analytic tool for locating individual tubes. Their vibrational modes have been detected with sub-μ lateral resolution. In particular, we present a detailed correlation of spectroscopic investigations and the geometry of thin bundles and individual single-wall CNTs using scanning confocal Raman microscopy and scanning force microscopy. This approach allows not only to distinguish between the separate CNTs, but also to perform spatially resolved Raman spectroscopy within a given bundle.

The choice of the substrate turned out to be crucial to obtain a reproducible signal over a reasonable number of scans. For example, on silicon wafers, irreproducible damage is caused to the substrate if a laser intensity of up to 1 MW/cm^2 is used for excitation, as is reflected in an increased broad fluorescence background. To avoid this problem, we depos-

[*] Dr. A. Mews, F. Koberling, Prof. T. Basché
Institut für Physikalische Chemie, Universität Mainz
D-55099 Mainz (Germany)
G. Philipp, G. S. Duesberg, Dr. S. Roth, Dr. M. Burghard
Max-Planck-Institut für Festkörperforschung
Heisenbergstr. 1, D-70569 Stuttgart (Germany)

[**] This work was supported by the BMBF under contract No. 03C0302B9. MB acknowledges financial support from the DFG.

  0935-9648/00/1608-1210 $ 17.50+.50/0

ited the CNTs on 15 nm thick Si_3N_4 membranes that are transparent at the laser excitation wavelength. In addition, the low roughness of the membrane surface (below 1 nm) is required for the detailed correlation between geometry and optical properties of the same objects. Moreover, the membranes are equipped with lithographically defined Pd/Au electrode arrays suitable for electrical transport measurements through individual nanotubes.[15] In the present work, the electrodes are used as position marker to identify the same nanotubes in the atomic force microscopy (AFM) and Raman experiments. In principle, however, the presented method and instrumentation opens the possibility of complementary structural, spectroscopic, and electrical transport investigations of the same molecular object.

An AFM image of the surface region which has been studied in detail is displayed in Figure 1a. To record an optical image, the same sample area is scanned through the excitation spot of the confocal microscope. Figure 1b results from the total scattering intensity when only the Rayleigh contribution is suppressed. The frequency distribution of the scattered light that can be seen in Figure 1c includes contributions from photoluminescence and Raman scattered light from the substrate, the electrode structures, or residues of the e-beam resist. To selectively detect the Raman contribution from the CNTs, the detector was placed behind a monochromator which was adjusted to 560 (±2) nm, i.e., to the G-line of the nanotubes, which is red-shifted by 1550–1600 cm^{-1}, with respect to the excitation wavelength. In this case, the Raman image of the individual CNTs can clearly be resolved as seen in Figure 1d.

A comparison between the Raman and the AFM image reveals that every bundle could be detected with the excitation wavelength of 514 nm or 488 nm (not shown). Since it was shown that, for the present tubes with diameters ranging from 1.1 to 1.4 nm, only semiconducting CNTs are resonantly excited at 514 or 488 nm,[16] this implies that all bundles contain semiconducting tubes.

During the investigations the tubes showed an extraordinary stability upon exposure to a laser excitation intensity of up to 1×10^6 W/cm^2, yielding a reproducible Raman signal over long periods of time without any detectable photobleaching. For example, bundles No. 6 and No. 2 were studied for more than 30 min—corresponding to an overall Raman signal of more than 10^9 photons—and could still be located in the Raman as well as in the AFM image. In this way, it was possible to record Raman spectra of isolated CNTs with a high S/N ratio, as exemplified by Figure 2. Figure 2a shows a survey spectrum in the frequency range from 300 to 3500 cm^{-1} and Figure 2b presents a high resolution spectrum with Lorentzian fits in the spectral range between 1200 and 1800 cm^{-1}. The band at 1348 cm^{-1} is attributed to disordered carbon (D-line) and the bands around 1600 cm^{-1}, which consist of at least three components, are the so called G-lines, i.e., tangential vibrations of carbon atoms arising from the optical phonons of the rolled-up graphite sheet. By improving the suppression of the strong Rayleigh contribution in the future, one will be able to record the radial breathing modes (RBMs) of the nanotubes between 100 and 250 cm^{-1}, from which the tube diameter can, in principle, be determined.[17]

The spectral shift and Raman intensity distribution among the different bundles is compared in Figure 2c and d, respectively. Obviously there are slight deviations in the peak centers and intensity ratios among the G-lines of different bundles, which necessarily leads to additional inhomogeneous broadening in bulk measurements. Most likely the different Raman frequencies are due to CNTs differing in diameter and/or symmetry within or among the CNT bundles. The intensity distribution in dependence of bundle height, shown in

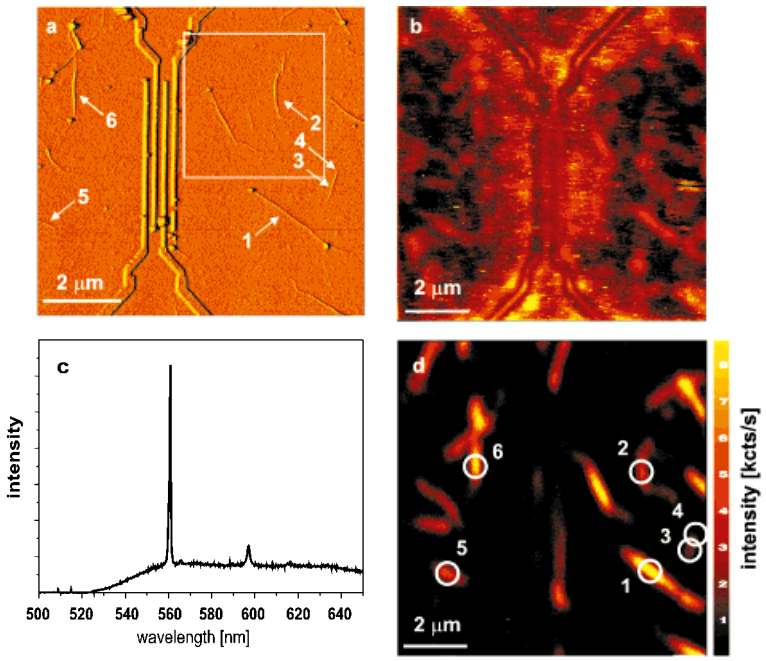

Fig. 1. Localization of carbon nanotubes (CNTs). a) AFM micrograph of CNTs on a Si_3N_4 membrane with lithographically defined electrode pattern. The electrodes were used as position marker for a detailed correlation between shape and Raman signal of the same CNTs. b) Confocal scanning image ($\lambda_{exc.}$ = 514 nm) of the same area as in (a). A holographic notch filter was used to reject the excitation light, but the electrode structure can clearly be resolved. c) Overall spectrum acquired during scanning image (b) by using a beam splitter and directing 50 % of the emission light to a spectrograph equipped with a CCD camera. A distinct Raman band originating from the CNTs is observed at 560 nm, and a second mode at 590 nm can be resolved above the broad background from the substrate. d) Confocal Raman image of the same area as in (a) with the detector placed behind a second exit port of the monochromator, which is adjusted to a center wavelength of 560 (±2) nm. Here, the individual bundles of CNTs appear clearly resolved with a high SNR. The labels mark the regions scanned to record the spectra in Figure 2. The white frame in (a) encloses the area displayed in Figure 3.

0935-9648/00/1608-1211 $ 17.50+.50/0

ADVANCED MATERIALS

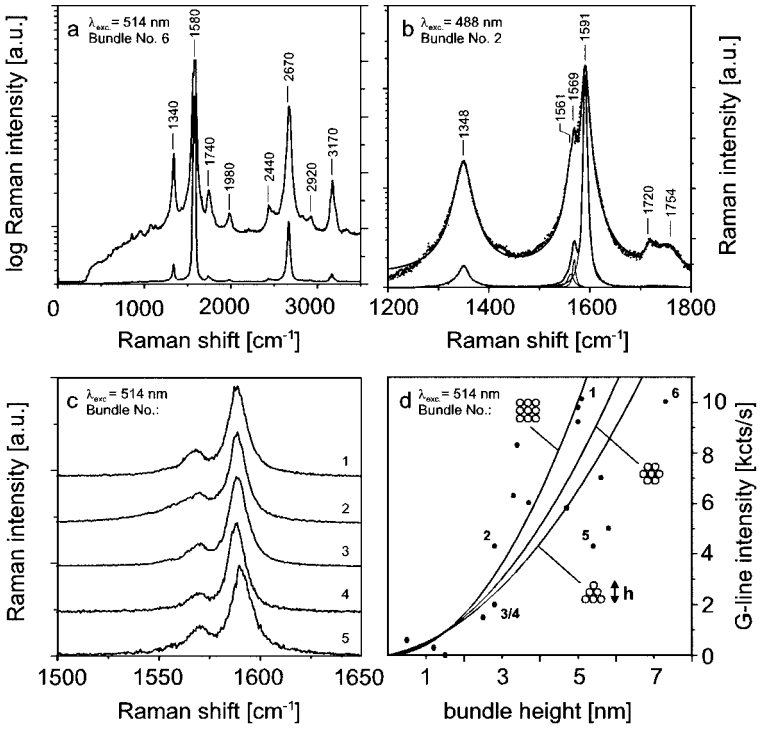

Fig. 2. Raman spectra of distinct bundles of CNTs. a) Survey spectra of bundle No. 6 without background subtraction on a logarithmic and linear scale ($\lambda_{exc.}$ = 514 nm). With the setup used no spectral information could be obtained below 300 cm^{-1} where the radial breathing modes (RBMs) of the CNTs are expected. The spectra show some structure in the mid frequency range between 300 and 1200 cm^{-1}, the D- and G-lines between 1200 and 1700 cm^{-1} (see b), and several additional bands, mostly overtones, above 1800 cm^{-1}. b) Raman bands and Lorentzian fits of bundle No. 2 in the frequency range between 1200 and 1800 cm^{-1}. The band at 1350 cm^{-1} is attributed to disordered carbon (D-line) whereas the G-line between 1500 and 1700 cm^{-1} consists of at least three components. c) G-line spectra of five different tube bundles shown in Figure 1. The spectra differ slightly in peak position and intensity ratios, which might be related to the presence of different kinds of carbon nanotubes. d) Correlation of bundle height and G-line intensity as taken from Figures 1a and d, respectively. The solid lines represent hypothetical Raman intensities calculated for close-packed CNTs (diameter: 1.5 nm) in a bundle of given cross-section, with each CNT equally contributing 900 cts/s. The pronounced deviation from this curve indicates that the Raman intensity is not only dependent on the bundle thickness, but also on other parameters such as the type of tubes or their geometry.

Figure 2d, was derived from the images in Figure 1a and d. If every tube contributed equally to the Raman signal (e.g., with a hypothetical count rate of 900 cts/s), and each bundle consisted of closed packed CNTs one would expect a quadratic dependence of the Raman intensity on the bundle height as shown in Figure 2d for different bundle geometries. The strong scattering of the data demonstrates, however, that additional parameters, such as local disorder, bending, and also the presence of different types of tubes might influence the intensity of the Raman signal.

A detailed comparison of Raman intensity and CNT structure is presented in Figure 3 for the subsection marked by a square in Figure 1a. The Raman image is presented as a multiple-color plot in order to highlight the high sensitivity of this method. Remarkable is the fact that the two CNT-bundles in line scan c are of the same height but exhibit Raman intensities varying by a factor of two as can be seen in line scan d. This observation could reflect different ratios of semiconducting to metal CNTs within those bundles, in agreement with the pronounced scattering of the data in Figure 2d. As an alternative explanation, the significant bending of the right bundle might also be responsible for the reduced signal.

A more detailed investigation reveals that the AFM line scan c shows three features, whereas the Raman line scan d shows only two signals, lacking a detectable signal from the middle object. For the latter, a height of ~1.5 nm is determined from the AFM section profile. This is interpreted as a single CNT, which apparently cannot be detected in the Raman image under the present conditions. On the other hand, line scan e again indicates the presence of single nanotubes by the AFM image, but these tubes do show the characteristic vibrational Raman modes at 560 nm. In view of the fact that metallic tubes cannot be resonantly excited at 488 or 514 nm,[16] we assume that the single tube in the center of line scans c and d is metallic, whereas the tubes along the line scans e and f are semiconducting.

The obtained data also allow the Raman cross section of single CNTs to be estimated. Briefly, the setup used exhibits a detection efficiency of the order of 1 %, i.e., one CNT yields approximately 10^4–10^5 Raman photons per second, or 10^{-15} W, when excited with an excitation intensity of 1 MW/cm^2. This results in an effective scattering cross section of about 10^{-21} cm^2, which is about five orders of magnitude lower than recently reported CNT cross sections in surface enhanced Raman scattering experiments[18] but still sufficient to localize single CNTs.

The fact that scanning confocal Raman imaging can be used to locate selected, individual CNT bundles—and even single CNTs—allows their vibrational properties to be studied under various conditions. This opens up the possibility of new, intriguing experiments, such as investigating the effect of chemical modification on the phonon structure of individual tubes. In addition, CNTs with kinks introduced by scanning probe manipulation could reveal the influence of the bonding geometry on the local vibrational properties. Moreover, transport measurements on electrically addressable CNTs could be complemented by Raman investigation, which includes the possibility of their in-situ characterization during device operation.

  0935-9648/00/1608-1212 $ 17.50+.50/0

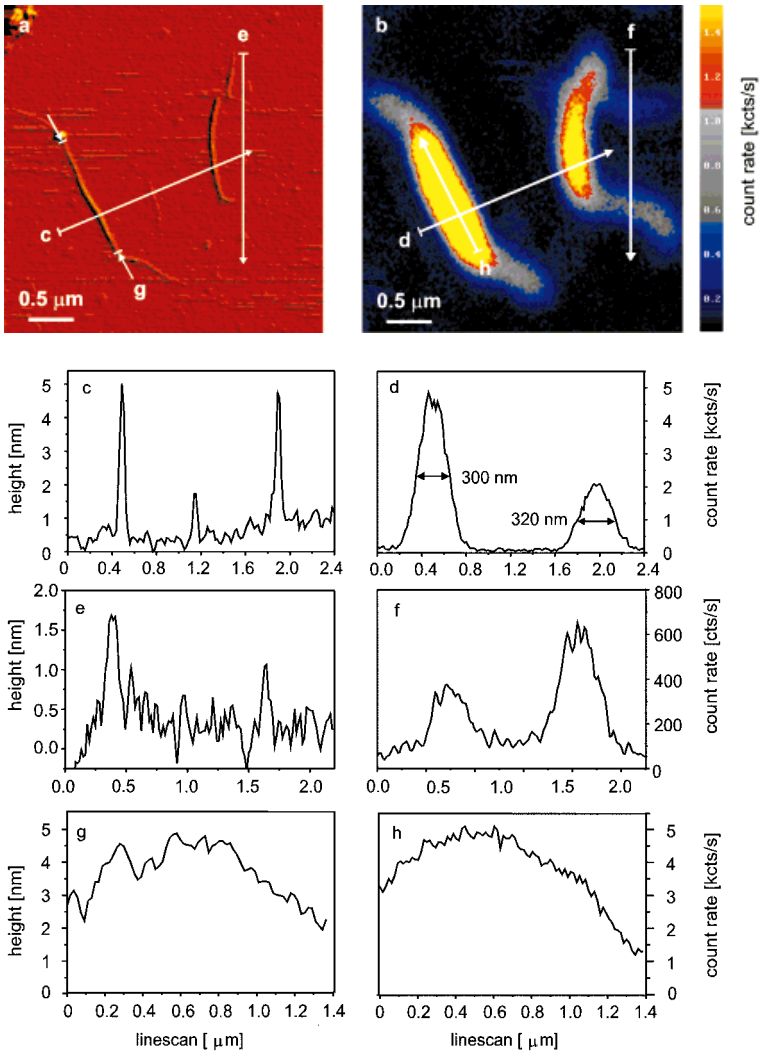

Fig. 3. Direct correlation between AFM and confocal Raman images. a) AFM subsection of the selected area marked in Figure 1a. b) Confocal image (based on G-line) of the same area as in (a). c–h) AFM and confocal line scans along the bars marked in (a) and (b), respectively. c,d) The AFM scan shows two bundles of CNTs, both with a height of 4–5 nm, and a third feature with a height of 1–2 nm that may be attributed to a single nanotube. The confocal Raman image exhibits no signal where the single tube is expected. e,f) The Raman image shows the presence of two tubes that can hardly be seen in the AFM micrograph, demonstrating the high sensitivity of this method. g,h) The line scans along one tube axis show that the CNT bundle is not homogeneously thick.

Experimental

SWNTs produced by the arc discharge method were purchased from CARBOLEX (Lexington, USA). The raw material was dispersed by ultrasonic treatment in an aqueous surfactant solution (1 wt.-% lithium dodecylsulfate), followed by chromatographic purification through a short column packed with CPG300 (Fluka). Prior to deposition of the SWNTs, the silicon nitride surface was activated by oxygen plasma treatment and modified with (3-aminopropyl)-triethoxysilane (0.1 wt.-% in water). Tubes were allowed to adsorb from a droplet of purified dispersion (~0.1 mg SWNT/mL) for 30 min. Subsequently the substrate was rinsed with water and blown dry. Silicon nitride membranes were fabricated by a procedure similar to that reported by Jacobs and Verhoeven [19]. AFM images were recorded with commercial silicon cantilevers in Tapping Mode (Digital Instruments Nanoscope IIIa).

Confocal scanning images and spectra were taken at room temperature using an inverted Zeiss microscope equipped with a piezo scanner (PhysicaI Instruments) and a high NA microscope objective (100×, NA = 0.9). In a typical experiment, circular polarized light (1 mW power) was focused down to a diffraction-limited spot size (diameter approx. $\lambda/2$) corresponding to an excitation power of the order of 1 MW/cm^2. To record an image, the sample was raster-scanned through the excitation spot and the Raman light was detected in back reflection and guided to an EG&G Avalanche photo diode (APD) while optical filters or a monochromator were used to eliminate scattered light. The images consist of 256×256 pixels with an integration time of 10 ms/pixel. The spectra where taken with an LN-cooled CCD camera (Princeton) behind a 500 mm single grating spectrograph (Acton) with a highest resolution of 2 cm^{-1}.

Received: July 3, 2000

[1] S. J. Tans, A. R. M. Verschueren, C. Dekker, *Nature* **1998**, *393*, 49.
[2] R. Martel, T. Schmidt, H. R. Shea, T. Hertel, P. Avouris, *Appl. Phys. Lett.* **1998**, *73*, 2447.
[3] J. Kong, N. R. Franklin, C. Zhou, M. G. Chapline, S. Peng, K. Cho, H. Dai, *Science* **2000**, *287*, 622.
[4] Z. Yao, H. W. C. Postma, L. Balents, C. Dekker, *Nature* **1999**, *402*, 273.
[5] M. S. Fuhrer, J. Nygard, L. Shih, M. Forero, Y.-G. Yoon, M. S. C. Mazzoni, H. J. Choi, J. Ihm, S. G. Louie, A. Zettl, P. L. McEuen, *Science* **2000**, *288*, 494.
[6] R. Saito, M. Fujita, G. Dresselhaus, M. S. Dresselhaus, *Appl. Phys. Lett.* **1992**, *60*, 2204.
[7] A. M. Rao, E. Richter, S. Bandow, B. Chase, P. C. Eklund, K. A. Williams, S. Fang, K. R. Subbaswamy, M. Menon, A. Thess, R. E. Smalley, G. Dresselhaus, M. S. Dresselhaus, *Science* **1997**, *275*, 187.
[8] A. Kasuya, M. Sugano, T. Maeda, Y. Saito, K. Tohji, H. Takahashi, Y. Sasaki, M. Fukushima, Y. Nishina, C. Horie, *Phys. Rev. B* **1998**, *57*, 4999.
[9] L. Alvarez, A. Righi, S. Rols, E. Anglaret, J. L. Sauvajol, *Chem. Phys. Lett.* **2000**, *320*, 441.
[10] D. W. Pohl, W. Denk, M. Lanz, *Appl. Phys. Lett.* **1984**, *44*, 651.
[11] *Single Molecule Optical Detection, Imaging and Spectroscopy* (Eds: T. Basché, W. E. Moerner, M. Orrit, U. P. Wild), VCH, Weinheim **1997**.

  0935-9648/00/1608-1213 $ 17.50+.50/0

ADVANCED MATERIALS

[12] S. A. Empedocles, R. Neuhauser, K. Shimizu, M. G. Bawendi, *Adv. Mater.* **1999**, *11*, 1243.
[13] G. S. Duesberg, W. Blau, H. J. Byrne, J. Muster, M. Burghard, S. Roth, *Chem. Phys. Lett.* **1999**, *310*, 8.
[14] G. S. Duesberg, I. Loa, M. Burghard, K. Syassen, S. Roth, unpublished.
[15] G. Philipp, M. Burghard, G. S. Duesberg, S. Roth, K. v. Klitzing, in *Electronic Properties of Novel Materials—Progress in Molecular Nanostructures* (Eds: K. H. Kuzmany, J. Fink, M. Mehring, S. Roth), New York **1998**.
[16] M. A. Pimenta, A. Marucci, S. A. Empedocles, M. G. Bawendi, E. B. Hanlon, A. M. Rao, P. C. Eklund, R. E. Smalley, G. Dresselhaus, M. S. Dresselhaus, *Phys. Rev. B*, **1998**, *58*, R16 016.
[17] D. Kahn, J. P. Lu, *Phys. Rev. B* **1999**, *60*, 6535.
[18] K. Kneipp, H. Kneipp, P. Corio, S. D. M. Brown, K. Shafer, J. Motz, L. T. Perelman, E. B. Hanlon, A. Marucci, G. Dresselhaus, M. S. Dresselhaus, *Phys. Rev. Lett.* **2000**, *84*, 3470.
[19] J. W. M. Jacobs, J. F. Verhoeven, *J. Microsc.* **1986**, *143*, 103.

Electrochemical Self-Assembly of Nanoporous ZnO/Eosin Y Thin Films and Their Sensitized Photoelectrochemical Performance

By *Tsukasa Yoshida*,* *Katsuyuki Terada*, *Derck Schlettwein*, *Torsten Oekermann*, *Takashi Sugiura*, and *Hideki Minoura*

Inorganic/organic hybrids are stretching the frontiers of materials research. Successful application in dye-sensitized solar cells (DSSCs)[1–4] has proven the usefulness of such materials, because ultrafast and efficient photoinduced electron injection into inorganic semiconductors can only be achieved by the dye molecules being chemically attached to the semiconductor surface.[5] DSSCs are truly molecule-based devices and should be regarded as different from inorganic/organic heterojunctions made by physical contact of bulk materials.[6] Indeed, self-assembly of an ordered monolayer of a Ru complex on a TiO_2 surface has been evidenced.[7] The key to success in DSSCs is the use of a porous inorganic semiconductor film, which results in a three-dimensional enlargement of the active inorganic/organic interface area.

In most previous studies, the photoactive materials in DSSCs were prepared by stepwise processing, that is, first, formation of porous films of inorganic semiconductors such as TiO_2 or ZnO by colloid coating and heat treatment, then, second, dye-adsorption by dipping the film in the dye solution.[1–4] While dye adsorption from solution should be effective for the formation of an ideal monolayer of dye molecules, active control of the crystallographic structure and pore size of the inorganic phase is difficult in the colloid coating process. The colloid process also requires the film to be sintered above 400 °C to cause necking of the colloid particles and thus improved electrical conductivity of the film; this limits the substrate to heat-resistant materials.

[*] Dr. T. Yoshida, K. Terada, Dr. T. Sugiura, Prof. H. Minoura
Environmental and Renewable Energy Systems (ERES) Division
Graduate School of Engineering, Gifu University
Yanagido 1-1, Gifu 501-1193 (Japan)
Dr. D. Schlettwein, Dr. T. Oekermann
Institut für Angewandte und Physikalische Chemie
Universität Bremen
NW 2, Postfach 330440, D-28334 Bremen (Germany)

Recently, we have developed a new and simple method to synthesize thin films of dye-modified ZnO by one-step cathodic electrodeposition from aqueous mixed solutions of zinc nitrate and sensitizing dyes.[8] As the whole material is self-assembled from solution in this process, the synergetic effect from the ZnO/dye boundary should be maximized, as a result of the chemical structures chosen by the constituent molecules, ions, and atoms. Because ZnO is grown by electrodeposition, its conductive nature is guaranteed without any heat treatment, thus providing a means to fabricate a flexible DSSC using conductive plastic substrates. In this communication, we report electrochemical self-assembly of ZnO/eosin Y thin films using the same strategy. Surface adsorption of eosin Y hinders the crystal growth of ZnO, leading to the automatic formation of the desired porous structure of the film. Eosin Y molecules condense at a sufficiently high concentration at the internal and external surfaces of the film to cause a specific intermolecular electronic interaction indicative of their ordered assembly. The deposited thin film has been found to perform as an efficient sensitized photoelectrode suitable for DSSCs.

Electrochemical reactions relevant to the film growth have been studied by cyclic voltammetry. Cyclic voltammograms measured in aqueous solutions of eosin Y, $Zn(NO_3)_2$, and their mixture are shown in Figure 1. An irreversible cathodic current gradually increases from around –0.7 V in a solution of $Zn(NO_3)_2$ (a). A thin film of ZnO is deposited during this process due to base generation by reduction of nitrate.[9] Reversible redox peaks centered at ca. –1 V (vs. SCE) are seen for the reduction of eosin Y (b). When both eosin Y and $Zn(NO_3)_2$ are present in solution, the cathodic peak corresponding to the reduction of eosin Y is shifted positively by ca. 0.2 V (c). At the same time, the anodic peak for reoxidation of eosin Y almost disappears, indicating that eosin Y is

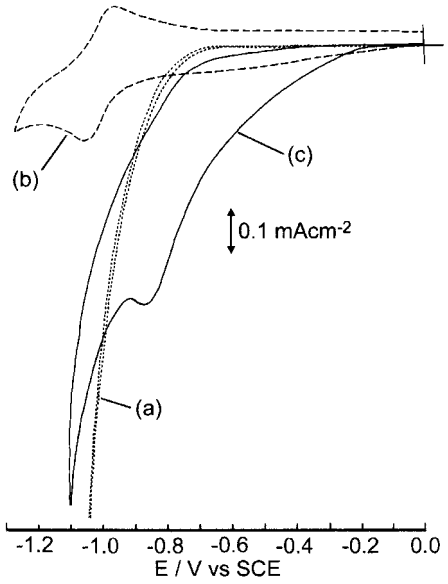

Fig. 1. Cyclic voltammograms measured at an ITO glass electrode in aqueous solutions of 0.1 M $Zn(NO_3)_2$ (a), 0.5 mM eosin Y + 0.1 M KCl (b), and 0.5 mM eosin Y + 0.1 M $Zn(NO_3)_2$ (c), maintained at 70 °C and saturated with Ar. Scan rate, 50 mV s^{-1}. All of the solutions had a pH of ca. 6.

  0935-9648/00/1608-1214 $ 17.50+.50/0